ADVANCED MATERIALS

Supporting Information

Observation of Multi-Directional Energy Transfer in a Hybrid Plasmonic–Excitonic Nanostructure

Tommaso Pincelli,* Thomas Vasileiadis, Shuo Dong, Samuel Beaulieu, Maciej Dendzik, Daniela Zahn, Sang-Eun Lee, Hélène Seiler, Yingpeng Qi, R. Patrick Xian, Julian Maklar, Emerson Coy, Niclas S. Mueller, Yu Okamura, Stephanie Reich, Martin Wolf, Laurenz Rettig, and Ralph Ernstorfer*

Observation of multi-directional energy transfer in a hybrid plasmonic-excitonic nanostructure Supplementary Information

Tommaso Pincelli* † Thomas Vasileiadis † Shuo Dong Samuel Beaulieu Maciej Dendzik Daniela Zahn Sang-Eun Lee Hélène Seiler Yingpeng Qi R. Patrick Xian Julian Maklar Emerson Coy Niclas S. Mueller Yu Okamura Stephanie Reich Martin Wolf Laurenz Rettig Ralph Ernstorfer*

† These authors contributed equally.

Dr. T. Pincelli, Dr. T. Vasileiadis, Dr. S. Dong, Dr. S. Beaulieu, Dr. M. Dendzik, Dr. D. Zahn, S.-E. Lee, Prof. H. Seiler, Dr. Y. Qi, Dr. R. P. Xian, J. Maklar, Prof. M. Wolf, Dr. L. Rettig, Prof. Ernstorfer
Fritz-Haber-Institut der Max-Planck-Gesellschaft, Faradayweg 4-6, 14195 Berlin, Germany
Email Address: pincelli@fhi-berlin.mpg.de, ernstorfer@tu-berlin.de
Prof. H. Seiler, Dr. N. S. Mueller, Y. Okamura, Prof. S. Reich
Freie Universität Berlin, Arnimallee 14, 14195 Berlin, Germany.
Dr. T. Pincelli, Prof. R. Ernstorfer
Institut für Optik und Atomare Physik, Technische Universität Berlin, Straße des 17. Juni 135, 10623 Berlin, Germany
Dr. T. Vasileiadis
Faculty of Physics, Adam Mickiewicz University, Uniwersytetu Poznanskiego 2, 61-614 Poznan, Poland
Dr. S. Beaulieu
Université de Bordeaux - CNRS - CEA, CELIA, UMR5107, F33405, Talence, France.
Dr. M. Dendzik
Department of Applied Physics, KTH Royal Institute of Technology, Hannes Alfvéns väg 12, 114 19 Stockholm, Sweden.
Dr. Y. Qi
Center for Ultrafast Science and Technology, School of Physics and Astronomy, Shanghai Jiao Tong University, 200240 Shanghai, China.
Dr. R. P. Xian
Department of Statistical Sciences, University of Toronto, 700 University Avenue, Toronto, M5G 1Z5, Canada.
Dr. E. Coy
NanoBioMedical Centre, Adam Mickiewicz University, ul. Wszechnicy Piastowskiej 3, PL 61614 Poznań, Poland.
Dr. N. S. Mueller
NanoPhotonics Centre, Cavendish Laboratory, Department of Physics, University of Cambridge, JJ Thomson Avenue, Cambridge CB30HE, United Kingdom.

Data	Mean	Standard Deviation	Variance	Skewness	Kurtosis	Median
Area	89.67 nm^2	93.93 nm^2	8823.18 nm^4	2.92	12.62	63.08 nm^2
Major	12.86 nm	7.38 nm^2	54.52 nm^2	1.07	0.61	10.87 nm
Minor	7.39 nm	3.43 nm	11.73nm^2	1.72	8.39	6.88 nm
Angle	$92.90°$	$55.63°$	$3094.61°^2$	-0.09	-1.29	$92.72°$
Circ.	0.72	0.19	0.04	-0.84	-0.31	0.78
AR	1.79	0.77	0.59	1.91	4.62	1.58

Table S1: Table reporting the values of the statistical analysis of particle shape. The total number of particles examined is 261, as observed in the overview image inset in S1. In each row, all the statistical parameters are reported for: nanoparticle area, the major and minor axis of the best fitting ellipse, the angle from horizontal of the best fitting ellipse major axis, the degree of circularity and the aspect ratio.

1 Transmission electron microscopy and particle shape analysis

High resolution Transmission electron studies were performed in an aberration corrected JEOL - ARM200F, working at an accelerating voltage of 200 kV. The samples were mounted in a reinforced beryllium holder (JEOL) and left in dark conditions and vacuum over night. Images were collected with a zone axis WSe$_2$ [0,0,1].

The following analysis shows that the Au covered area fraction is 50%, and that in-plane particle size follows a skewed distribution whose median is 10 nm. The nominal thickness of the nanoparticles is estimated to be around 2 nm. The epitaxial relationship is evident from the static diffractogram reported in Fig. 1d of the main text, where single crystalline Bragg peaks from Au are observed as a replica for each WSe$_2$ substrate peak. The slight offset between the peaks results from the mismatch between the two lattice structures that, combined with the large inelastic mean free path of Au atoms on WSe$_2$ surface, is at the origin of the Vollmer-Weber growth resulting in the self-assembled nanostructures [1].

The particle shape analysis was performed using a TEM microscopy image from the same sample and instrument as in Fig. 1d of the main article. The image spans a range of 180 nm x 213 nm. The image has been thresholded to define the islands. The result is reported in the inset in Fig. S1. The Au islands are in white. The area and circularity of the nanoparticles were extracted using the ImageJ automated analysis software. Circularity is given by $4\pi * Area/(Perimeter)^2$. The nanoparticles were also fitted with ellipses, allowing to extract several parameters: major and minor axes, the angle of the major axis with respect to the horizontal (Angle), and the aspect ratio. The results are summarized in Tab. S1 and Fig. S1.

From Tab. S1, emerges a simplified average shape of thin, ellipsoidal disks with major axis around 13 nm and minor axis around 7 nm, elongated in randomly oriented directions. By looking at the distributions of Fig. S1, however, it is clear that the sizes and shapes of the nanostructures span a vast range of scales, thus making necessary a true-to-shape finite-element modelling, as reported in Fig. S2.

2 Localized fields and finite elements calculations

We report the distribution of the field enhancement $|E|/|E_0|$ (where $|E|$ is the modulus of the electric field in the heterostructure and $|E_0|$ is the field in absence of Au). This scalar quantity is calculated by performing finite element, frequency domain calculations on a model
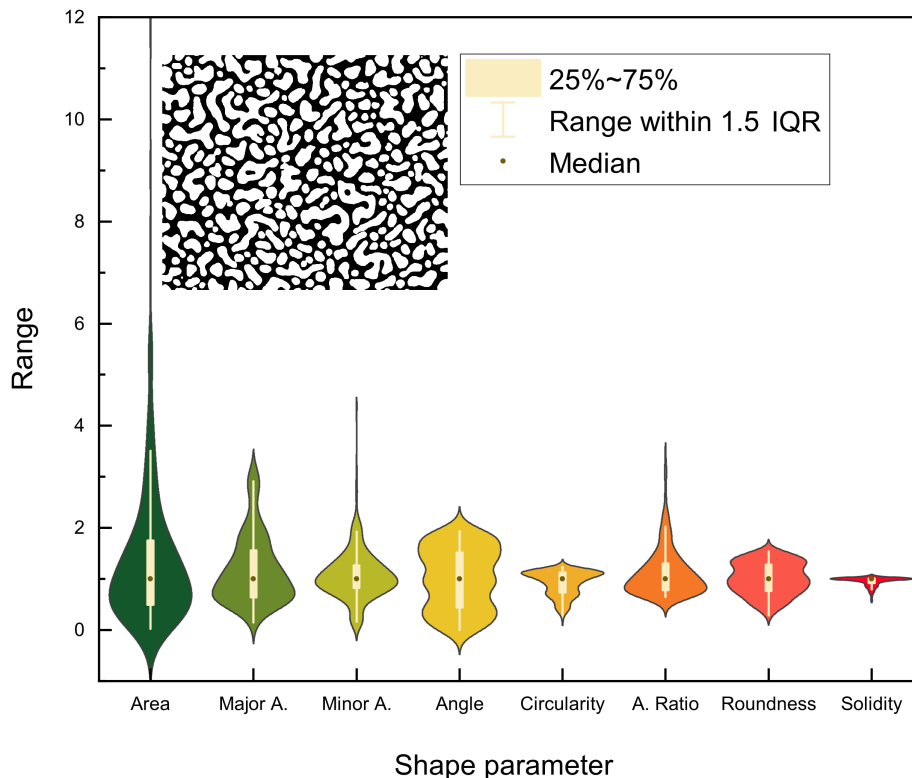
Figure S1: Violin plot showing the distributions of the values of each parameter. The vertical scale of each distribution has been normalized to the mean value, reported in Tab. S1. The "range" axis thus represents the extent of the distribution in units of the mean value. The thick line encloses the range between 25% and 75% of the mean value, while the thin line marks the range within 1.5 times the interquartile range.

Au/WSe$_2$ heterostructure (see also Methods in the main article). The dielectric functions were from tabulated data: Au from [2] and WSe$_2$ from [3]. To calculate $|E_0|$, the calculation was repeated with identical settings except for the refractive and absorption index of Au, that were set to the ones of vacuum instead. The total modulus was calculated for both E and E_0 3D vector fields, and their ratio determined to produce the three-dimensional scalar field of field enhancement. The field is then sampled by slicing the model volume with a plane parallel to the Au/WSe$_2$ interface. In the following images, we report the field enhancement on two planes above and below the interface at various different wavelengths.

The slices above the surface (Fig. S2 a,c,e,g,i) show the field enhancement within the nanoislands and in the vacuum space between them. At 400 nm the excitation frequency is above the Au interband transtion, Au absorption becomes significant, and the field enhancements are largely confined outside of the nanoparticles. With longer wavelengths, we observe significant field enhancement also within the nanoparticles as the bulk shape of the particle becomes more relevant in determining the dominant plasmonic modes. In the 800-1030 nm range explored in the experiments, the generation of hot electrons is therefore enhanced by localized plasmonic excitations that affect a large fraction of the volume of the particle and depend strongly on the particle shape. The slices below the surface (Fig. S2 b,d,f,h,j), on the other hand, indicate how the field tailoring produced by the nanostructure propagates within the WSe$_2$ substrate. Above the semiconducting direct bandgap, the field enhance-
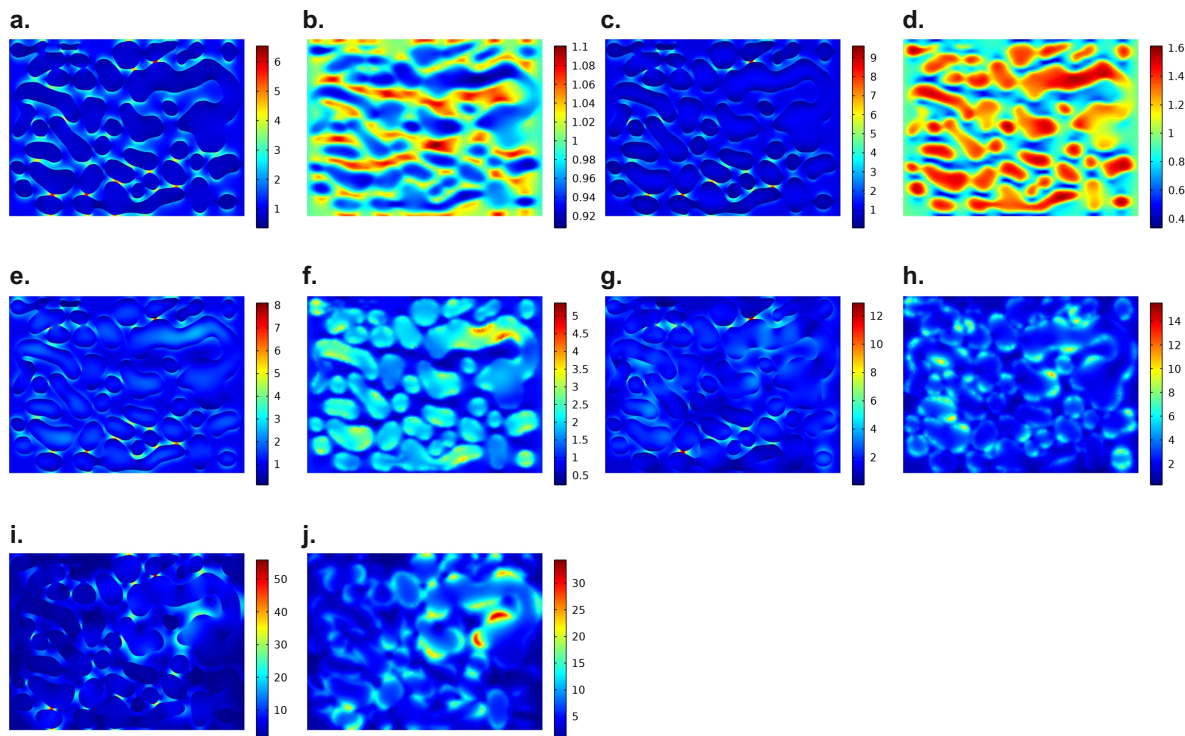
Figure S2: **Electric field enhancement at various wavelengths.** a.-b. Electric field enhancement in Au nanoislands on WSe$_2$ 2nm above (a.) and 1 nm below (b.) the interface, with 400 nm excitation. c.-d. Same, but for 800 nm excitation. e.-f. Same, but for 860 nm excitation. g.-h. Same but for 1060 nm excitation. i.-j. Same, but for 1200 nm excitation.

ments within WSe$_2$ are small. At 400 nm light is strongly absorbed also by the nanoparticles, and we observe only weak enhancement in the gaps between them (Fig. S2 b). At 800 nm, the particles act as field concentrators and a weak enhancement is created under their footprint (Fig. S2 d). At longer wavelengths the enhanced field can propagate more freely in the semiconductor, and we observe large field enhancements generated by the edges of the particles whose shape resonate with the excitation wavelength (Fig. S2 f,h,i). This therefore suggests that, as we move towards longer wavelengths, we increase the probability for multiphoton processes in the semiconductor due to large field enhancements.

3   Band structure calculations with density functional theory

For the overlayed curves in Fig. 2b (main article) and Fig. S4 c, we performed density functional theory (DFT) calculation of WSe$_2$ and Au with the projector augmented wave code GPAW [4] using GLLBSE xc-functional, separately. The GLLBSC is an orbital-dependent exact exchange-based functional that is well suited for the description of noble metals [5, 6]. While DFT+U might provide a better description of the d-states of Au [7], we opted for a parameter-free functional that still provides a good, general description of Au(111) band-structure, as the d-bands are not directly involved in the dynamics discussed in this work.For Au, we performed a slab calculation, with 5 ML Au(111) (2.5 nm) thickness and 15 Å vacuum thickness. The choice of a slab calculation allowed us to obtain an ab-initio description

of the Shockley surface state.We used a Monkhorst-Pack sampling of the Brillouin zone with (12x12x1) points. The plane wave energy cutoff was at 600 eV, the occupation defined by a Fermi-Dirac distribution with 0.01 eV width. For WSe$_2$, we performed a bulk calculation with (12x12x12) Monkhorst-Pack sampling, plane wave energy cutoff at 600 eV and occupation defined by a Fermi-Dirac distribution with 0.01 eV width. The bandpath was selected to cut the Brillouin zone at k$_z$=0. All DFT calculations are performed with the projector augmented wave code GPAW using fully realtivistic - thus including spin-orbit coupling - plane wave basis sets and PAW potentials version 0.9.2.

4   Weak hybridization of the electronic states

Besides the general agreement to the DFT calculations for the two separate materials reported in Fig.2 b and Fig. S4 c, we have attempted to further investigate the effects of interfacing on the electronic structure of the two materials.

The first evidence is the absence of any variation in the shape of the core-level peaks shown in Fig. S4 a,b, which would display the evolution of substructures arising from different valence states of the atoms in the presence of alloying, chemical bonding or oxidation. The peaks of Selenium (not shown), were also measured and do not show any significant lineshape change.

Furthermore, it is possible to inspect the valence band with a more critical insight. Two features have been identified in [8], where monolayers of MoS$_2$ on bulk Au(111) were studied, that showed a deviation between the suspended theoretical bandstructure of ML MoS$_2$ and the one observed on the Au(111) substrate.

The first is a flattening and shift towards lower binding energies of the band at the Γ point. This phenomenon arises because the orbital character in this region is formed predominantly by the chalcogenide p$_z$ orbitals and transition metal d$_{z^2}$ and d_{yz} orbitals, and is therefore sensitive to out-of-plane chemical interactions. In [8], the MoS$_2$ valence band top at Γ is found to be shifted 310 meV to higher binding energies due to hybridization with Au d-band continuum. No such effect is observed in the present case of thin Au(111) overlayers on WSe$_2$, as demonstrated by Fig. S3 a,b.

Another region where the effects of interfacing are seen is the M point. Indeed this represents a time-reversal invariant momentum point, where the combination of crystal symmetry and time-reversal symmetry enforce spin degeneracy. The lowest binding energy band, that is spin-orbit split at the K points, is therefore degenerate at the M point. In the case of ML MoS$_2$ on Au, such degeneracy is not observed, owing to the suppression of momentum-matching constraints at the edge of the Brillouin zone caused by strong hybridization with the Au states. In the present case, the band at the M point appears to be spin degenerate as shown in Fig. S3 c,d.

5   Core-level photoemission and band alignment

The band alignment between Au and WSe$_2$ can be explored with very precise insight using photoemission data. Firstly, we consider the shifting of the core levels. We measure the Au 4f and W 4f peaks for the separate surfaces of Au(111) and WSe$_2$(0001), and for the heterostructure. To gain a deeper insight in the effects of Au coverage, we also measured at two different nominal Au thicknesses, 12 Å and 36 Å. The results are reported in Fig. S4.
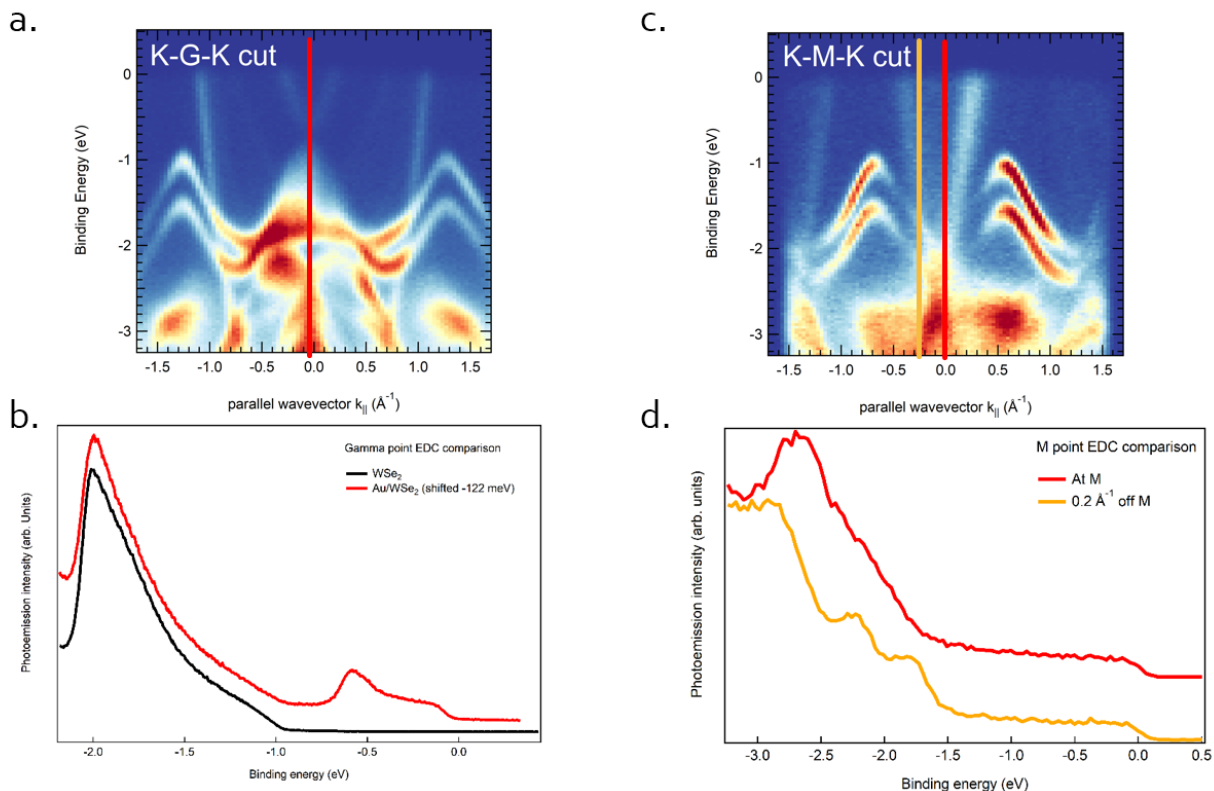
Figure S3: **Weak interaction modifications of the electronic structure.** a. Static bandstructure cut along the K-Γ-K direction. Red line shows the EDC cut shown in panel b. b. EDC cuts at the Γ point for bare WSe_2 (black) and Au/WSe_2 (red). The red EDC has been shifted by 122 meV to compensate the effects of band alignment. c. Static bandstructure along the K-M-K direction. The yellow and red lines show the respective EDC cuts shown in panel d. d. EDC cuts at M (red) and slightly off M (yellow), showing how, moving toward the M point, the double peaked structure around 2 eV becomes a spin-degenerate feature around 2.5 eV.

Considering the electron affinity X_{WSe_2}=4.1 eV, the Fermi edge position Φ=4.4 eV, and the indirect bandgap E_g=1.47 eV, in a freshly cleaved WSe_2 (0001) surface the virtual Fermi edge position is just 300 meV below the conduction band minimum, in line with the n-type behaviour observed for intrinsic WSe_2. In this condition, contacting the Au(111) facet, of work function Φ_{Au}=5.5 eV, would cause a shift of the Fermi level in WSe_2 of $\Delta\Phi$=1.1 eV. This would lead to the Fermi level being very close to the valence band, just 100-70 meV above. However, this is not what is observed. Indeed, we only observe a shift of 170±5 meV of the WSe_2 bands when Au is evaporated on the surface. This indicates that the band bending is strongly suppressed and the Fermi level is moved to only 0.47 eV below the conduction band.

Considering the Schottky-Mott theory of contact potential, the Fermi level would be expected to be energetically near the VBM. However, owing to the work function reduction observed in Au nanoparticles [9], the Fermi level is closer to the conduction band minimum of WSe_2, with Schottky barrier $\Phi_e = 0.470 \pm 0.005 eV$ for electrons (ESB) and $\Phi_h = 1.000 \pm 0.005 eV$ for holes (HSB) [10].

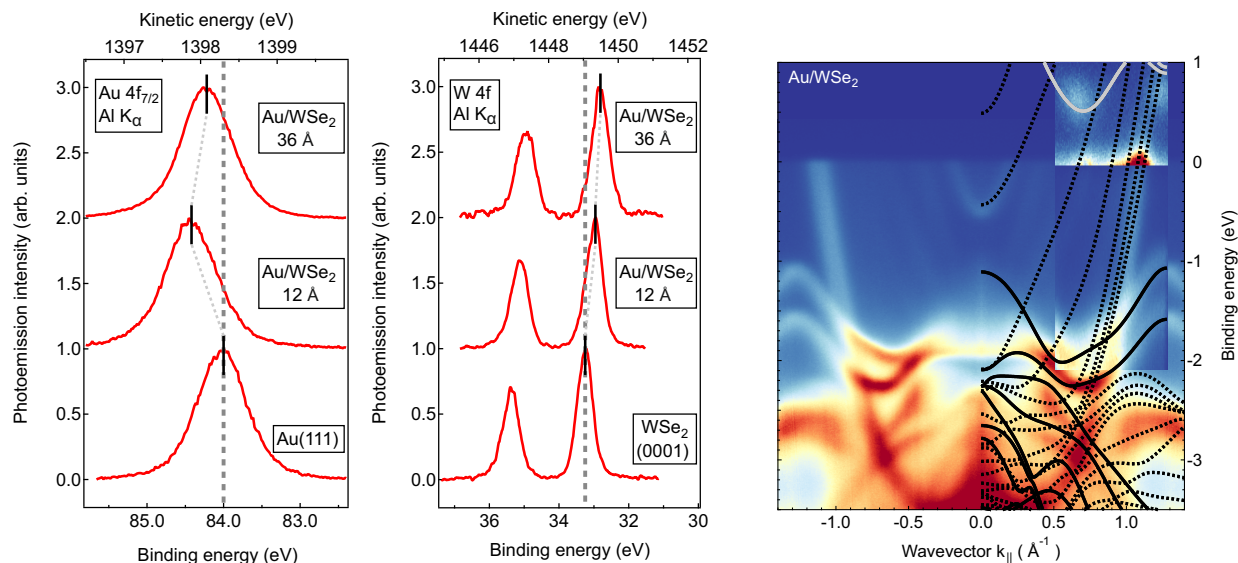Such suppression results from the nanoscale structure of Au. In these conditions, the

Figure S4: **Band alignment.** a. Au $4f_{7/2}$ peak at room temperature for bulk Au(111), for 12 Å Au on WSe_2 and for 36 Å Au on WSe_2. Dashed line marks the reference for Bulk. Black markers indicate peak position as obtained by fitting with Doniach-Sunjic lineshape convolved with a Gaussian. b. W 4f doublet at room temperature for freshly cleaved $WSe_2(0001)$, and the heterostructure at two coverages reported in panel a. Dashed vertical line marks the reference for the bulk, black markers indicate the peak position as obtained by fitting Voigt lineshapes. c. Combined image of static ARPES, a time-resolved ARPES snapshot at t=20 fs (inset), and bandstructure calculations. note that the tr-ARPES snapshot has been aligned energetically considering the fact that the Fermi edge is shifted by -40 meV in the transient signal.

nanoparticles have a significantly reduced work function. This is clear from the Au 4f shifts in Fig. S4 a. When 12 Å Au are deposited on WSe_2 surface, the $4f_{7/2}$ peak shifts about -420±8 meV to higher binding energies, owing to the reduced work function. Upon further increase of the thickness to 36 Å, the film still remains disconnected, but the islands grow, thus getting closer to the bulk work function: the Au 4f shift decreases to -220±7 meV. Au 4f peak positions are determined by fitting the $4f_{7/2}$ with a Doniach-Sunjic lineshape, after Shirley background subtraction of the whole 4f doublet. Errors are propagated from the standard deviation on the fit result.

As the islands are disconnected, a static electric dipole also builds at the interface, that further contributes to the band bending suppression. This is clear from the monotonous positive shifting of the W 4f peaks in Fig. S4 b: at 12 Å, it is +270±8 meV, while at 36 Å, it is +440±9 meV. W 4f peak positions are determined by fitting the $4f_{7/2}$ with a Voigt lineshape, after Shirley background subtraction of the whole 4f doublet. Errors are propagated from the standard deviation on the fit result.

It does not appear that Au evaporation produces significant chemical interaction with WSe_2, as the core-level lineshapes are remarkably identical to each other, aside from the aforementioned shifts. There are also no significant hints of hybridization in the bandstructure, as explained in the previous section.

Finally, we have one more method to pinpoint the band alignment, i.e. the use of time-resolved ARPES. As it can be readily seen in the overlay of Fig. S4 c, the Fermi edge is indeed about 0.5 eV away from the bottom of the conduction band. More precisely, we find the

valence band minimum 612 ± 2 meV above the Fermi edge. However, we have to consider that at the time delay in which we have sufficient population of the bands (reported in the inset in Fig. S4 c) we also have a transient relative shifting of the charge state of the two materials, that adds up to 140 ± 5 meV (see Fig.3a). The equilibrium position of the conduction band minimum is therefore 472 ± 5 meV above the Fermi level, and this constitutes the electron Schottky barrier.

6 Lifetime of Σ valley population

To perform the fits of the Σ valley population, we built a fitting function that consists of a double exponential decay convolved with a gaussian instrument response function.

This allowed us to isolate the intrinsic and interfacing-dependent timescales.We first considered a dataset measured for the WSe_2 bare surface in the same experimental conditions, but with a much wider delay range, up to 200 ps. Fitting the population of the Σ valley with the convolved double exponential (with fixed gaussian FWHM of 40 fs), returned two timescales: 1502 ± 78 fs and 31 ± 2 ps. The result is reported in Fig. S5.

The first time-constant seems rather short with respect to the dark exciton lifetime or defect recombination times reported in literature [11]. It thus might be attributable to dark exciton diffusion in the bulk, away from the probing depth of ARPES.

In the dataset discussed in the main text, the delay range is much smaller, so only the short timescale is relevant. It is evident from the data, however, that a second, shorter timescale arises in the heterostructure. We thus considered the curve of Au/WSe_2 at low temperature, showing the fastest dynamics. By fixing the longest timescale to be 1502 fs, we obtain the shortest to be 240 ± 28 fs. The amplitude of the fast decay is $72\pm2\%$ of the signal. These two timescales are sufficient to fit the other two curves in Fig.3c with high reliability by only changing the ratio between them. The one for Au/WSe_2 at RT is fitted by reducing the short timescale to the $36\pm8\%$ of the signal, while the pure WSe_2 converges with only $2\pm10\%$ of the short timescale, indicating that it is well fitted by the single exponential of 1.5 ps.

7 Fluence dependence of Σ valley population

We discuss here the procedure to extract data from the 1030 nm pump dataset. The measurement was performed at fixed delay of +400 fs, i.e. after the ultrafast charge transfer mechanisms have taken place, thus in the condition to observe the exciton population generated in WSe_2 by two photon processes. The fluence was changed from 0.28 to 2.34 mJ/cm^2.

In these conditions, the electronic temperature is between 1500-2000 K and, while still lower than 5800 K (the minimum electron Schottky barrier, which also increases transiently), this is sufficient to produce a background signal from the Au electrons that needs to be removed in order to isolate the Σ valley population.

The shape of the Au bands in the momentum region corresponding to the WSe_2 sigma valley (between the red lines in Fig. S6 b) is such that a fluence dependent fit of the Fermi edge is not reliable at high fluences. For this reason, an exponential decay background was used above the Fermi level. A typical result is shown in Fig. S6 a. However, given the less physically solid choice of fitting function, a routine was employed to improve statistical
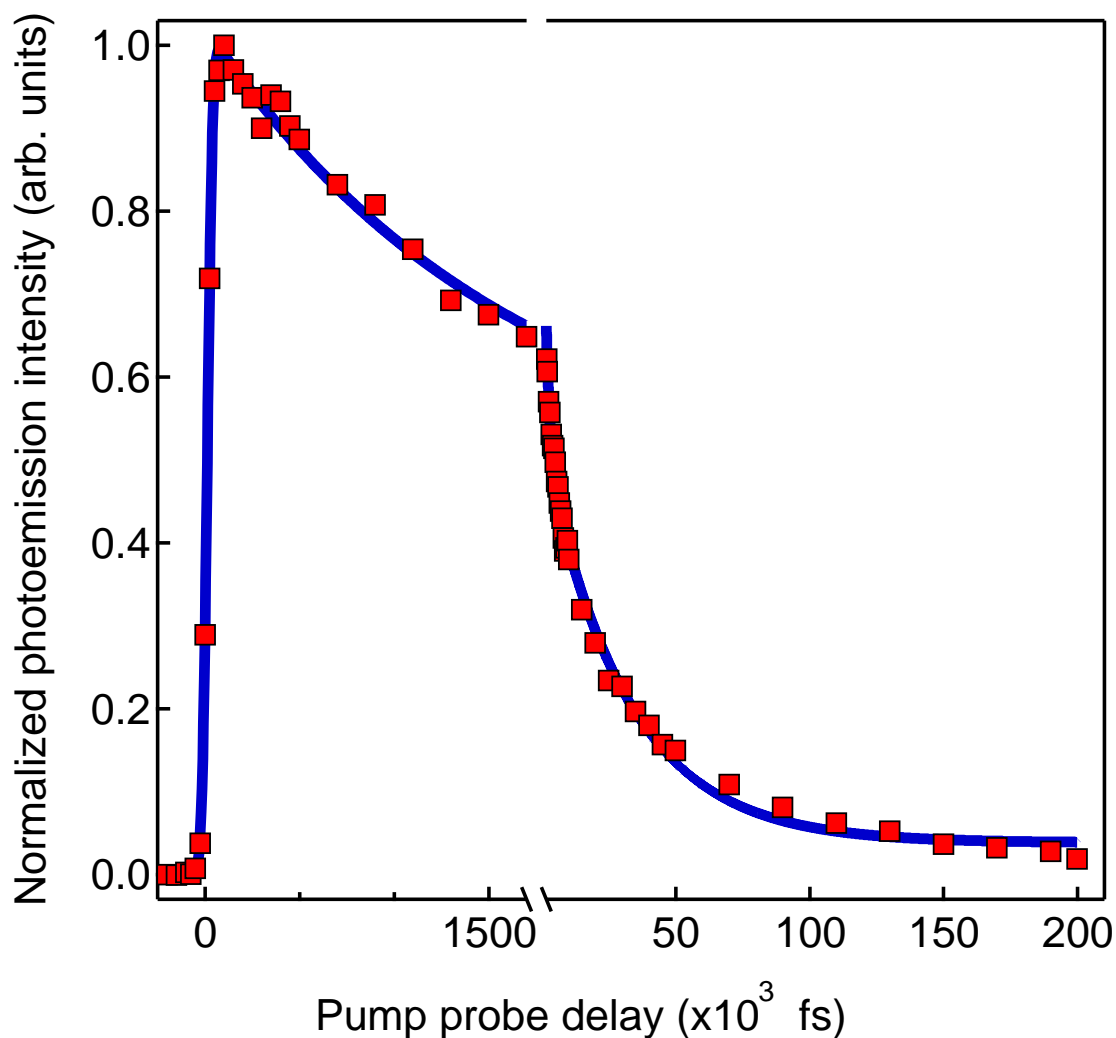
Figure S5: **Long delay Σ valley population for pure WSe$_2$.** Combination of data and fit for pure WSe$_2$ measured with 800 nm pump, 0.6 mJ/cm^2 fluence. The long delay range shows a two timescales decay.

accuracy: for each point of the fluence dependence, the background fitting and subtraction was repeated six times, with slightly different choices of fitting intervals. The error bar in the data reported in Fig.3d are determined as the standard deviation of the result distribution.

Fermi edge extraction was instead carried out in the momentum range corresponding to the sp-band, marked by black lines in Fig. S6 b. In this region, the Fermi distribution could be fitted reliably at all fluences, and the error reported is the standard deviation obtained by least square fitting.

Finally, we report here a plot of the integral of the Fermi-Dirac electron distribution above the energy levels corresponding to the Σ and K valleys. If we exclude the lowest fluence, that produces a negligible increase in the electronic temperature, and fails to produce a detectable population above the WSe$_2$ valence band energy, as the hot electron population
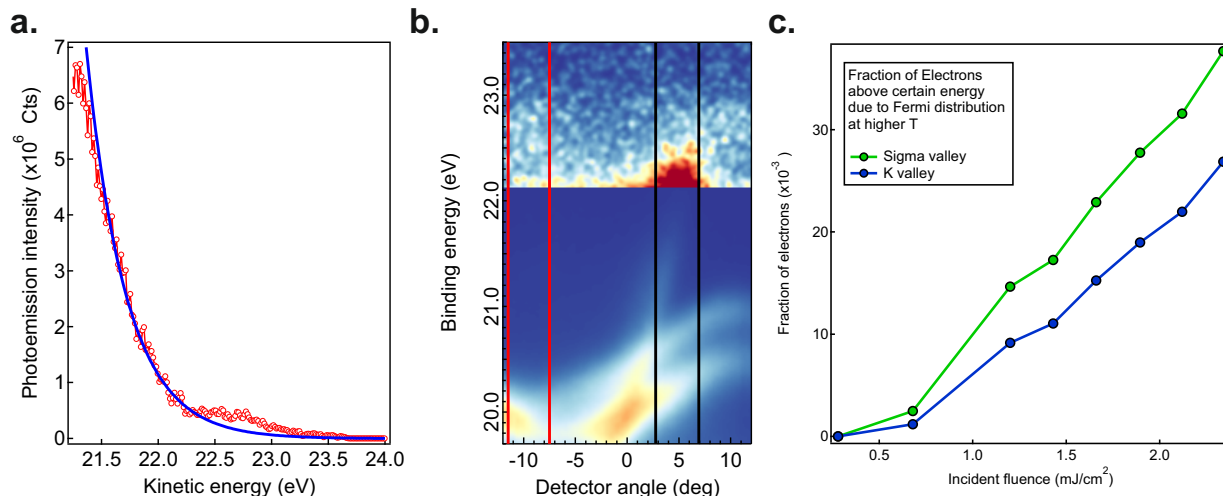
Figure S6: **Analysis of 1030 nm measurements.** a. Typical result of background fitting for the extraction of fluence dependence of Σ valley population. The fluence is 1.66 mJ/cm^2, the delay $+400$ fs. The red circles show the data as obtained from tr-ARPES signal integration in the momentum range shown in panel b by the red lines. The blue curve shows the exponential background. b. tr-ARPES map with 1030 nm pumping. The red lines mark the range of integration for the EDC used for Σ valley population extraction, while the black lines show the range for Fermi edge fitting. c. Plot of the integral of the Fermi-Dirac distribution between the energy of the Σ and K valley and infinity, as a function of the electronic temperatures corresponding to the fluences used in Fig.3d.

scales linearly in this range of fluences.

8   Negligibility of Seebeck effect and surface photovoltage

Regarding the shifts observed in Fig. 3b, we have examined if they result from a combination of surface photovoltage and Seebeck effect (transient voltages due to transient temperature gradients). Both effects can be ruled out.

On Bare WSe$_2$ the bands shift by less than 7 meV in any condition of fluence, pump wavelength and temperature, thus ruling out any intrinsic effects of the semiconductor. The effect is also too short-lived with respect to classic surface photovoltage.

The Fermi edge of Au does not shift due to temperature changes. This is what is measured by the Seebeck coefficient, which for Au is below 3 μV/K up to 2500K. This means that a change of temperature of 3000 K results in a shift of less than 9 meV. We observe shifts of 20 meV (electronic temperature change ΔT_e=700 K, Seebeck shift 2 meV), or 40 meV (ΔT_e=800 K, Seebeck shift 2.4 meV) or finally of 200 meV (ΔT_e=3000 K, Seebeck shift 9 meV).

9   Energy flow across the interface

The band alignment suggests that under photoexcitation with photon energies below the Au interband threshold (<2 eV) plasmon-generated hot electrons can be injected at much larger rates than hot holes thus dominating the charge transfer mechanism. The still sizable

Schottky barrier suppresses the diffusion of thermalized electrons across the interface for low photoexcitation fluences (<10 mJ/cm^2).

At higher pump photon energies, it becomes possible to excite large populations of deep lying holes with long lifetimes, giving rise to complex energy exchanges that may tip the balance in favour of hot-hole injection [12, 13], but this falls beyond the scope of our work. We will restrict our discussion to pump photon energies below the A exciton resonance of bulk WSe$_2$ (1.626 eV at room temperature [14]).

A simple electrostatic calculation considering the peak chemical potential shift $\Delta E = 40$ meV and the nanoparticle capacitance $C = 3$ aF allows to calculate the net number of injected electrons as $n = \Delta E \cdot C \leq 1$. Combining this with the number of absorbed photons per nanoparticle at 800 nm, considering an absorption of 0.1% of the nanoparticles (from the FDTD calculations), we get a quantum efficiency (in gap photon to hot electron in WSe$_2$) of about 2%, in line with other reports on similar systems. We argue, however, that the flow of energy carried by unbalanced charges is smaller than the total energy flow across the interface, owing to the fact that both HSB and ESB are smaller than the photon energy at any pump excitation wavelength.

10 Probing depth of ARPES

When considering photoemission data from a heterogeneous sample, it is important to remember that the probing depth of ARPES is extremely short, in the range 10-5 Å at the photon energies employed in the current experiment (21.7 eV). This means that the experiment is predominantly sensitive to the top facet of the Au islands and the open areas of WSe$_2$, while the interface between the islands and the semiconductor is more challenging to access experimentally.

Our analysis overcomes this hurdle in two ways. Firstly, we focused on observables that do not require the direct observation of the spatial region below the particle. The band alignment analysis is supported to a very high degree of consistency by core-level data (more bulk sensitive) and theoretical calculations. The dynamics is explored considering the electronic temperature of Au, its chemical potential, the band positions in WSe$_2$, i.e. properties that can be considered homogeneous at the scale of a single particle or gap (approx. 10 nm) at these timescales (> 10 fs). Secondly, to assess for example population dynamics, we put ourselves in a condition where we are intrinsically selective of the carriers generated by injection by tuning the excitation wavelength.

The latter strategy is viable because the signal does carry information on the WSe$_2$ Bloch eigenfunctions below the islands, at least to a degree. A careful comparison of the MDCs of the bands of bare WSe$_2$ to the same states in the heterostructure, shows that they are broadened to a FWHM of 0.1 Å^{-1}. This corresponds, in real space, to approx. 10 nm, i.e. the average gap between the islands, suggesting that, in a three-step picture of photoemission, the confinement of the ARPES wavefunction happens in the final step. The information carried by the angular distribution of the photoelectrons, however, relates to the coherence length of the electron wavepacket in the solid within the plane. In this direction, the inelastic mean free path of the electrons is rather large, and no significant losses are encountered at such energies. Therefore, while the signal arising from below the nanoparticles might be suppressed, the ARPES signal should still carry information regarding the interface.

11   Non-thermal electrons

As discussed in [15], in the femtoseconds immediatley subsequent optical excitation the electronic distribution in the proximity of the Fermi edge assumes a shape that is not described by a Fermi-Dirac distribution. It is instead formed by a Fermi-Dirac distribution of higher temperature, with superimposed steps with exactly the width of the photon energy $\hbar\omega$. A step-wise decrease in the range $[E_f - \hbar\omega, E_f]$ as electronic states below the Fermi level are depleted, and a step-wise increase in the range $[E_f, E_f + \hbar\omega]$. The steps might have a more complicated structure, arising from the details of the DOS of the metal within $\hbar\omega$ from the Fermi level. Aluminum, for example, is theoretically predicted to display a small peak in each step, owing to a local maximum in the DOS just below E_f. The DOS of Au, instead, is rather flat until 2 eV below E_f, thus producing flat, step-like features. We investigate the existence of such non-equilibrium distributions for two reasons: to ensure that large non-thermal distributions of electrons do not affect our fitting of the Fermi edge (in particular the energy position), and to understand the role of non-thermal electronic distributions in the early dynamics of the heterostructure.

As can be seen in Fig. S7, both the fits of the Fermi edge return no significant non-thermal contributions superimposed on the Fermi-Dirac distribution. The fits have been performed by fitting a Fermi-Dirac distribution convolved with a Gaussian distribution to simulate experimental distribution. The width of the Gaussian was obtained by fitting the negative delays while constraining the temperature to be 70 K, and found to be 150 meV. Then, the Fermi edge was fit leaving the amplitude, the energy position and the temperature as free parameters. The fits of the sp-band have been performed in a rather restricted energy range to avoid contamination of the signal with the intensity of WSe$_2$ conduction band K points.

The lack of obvious non-thermal distributions, or in general of strong trends in the residuals of the fits, indicates that the fitted Fermi edge position discussed in the manuscript is reliable. More subtle is the interpretation of the role of non-thermal populations in the dynamics of the heterostructure. While we would expect to observe non-equilibrium distributions at these incident fluences and delay ranges, their absence might suggest that all hot carriers are injected in the semiconductor. However, to assess the non-thermal component of the electronic distribution directly, it would be necessary to have a signal-to-noise ratio in the residuals much higher than the one of the current experiment. Such dedicated experiment falls beyond the scope of the current work.

12   Two temperature model for electron-lattice equilibration in Au

In Fig. 3a of the main article we compare the experimental results to the prediction of the two temperature model (2TM)[16, 17]. A simple two temperature model was set-up to create a reference of bulk Au without charge-transfer, in the same conditions of excitation density. The equations employed are:

$$(\gamma_e \cdot T_e) \cdot \frac{\mathrm{d}T_e}{\mathrm{d}t} = -G_{e-ph}(T_e - T_l) + P(t) \tag{1}$$

$$C_l \cdot \frac{\mathrm{d}T_l}{\mathrm{d}t} = G_{el-ph}(T_e - T_l) \tag{2}$$
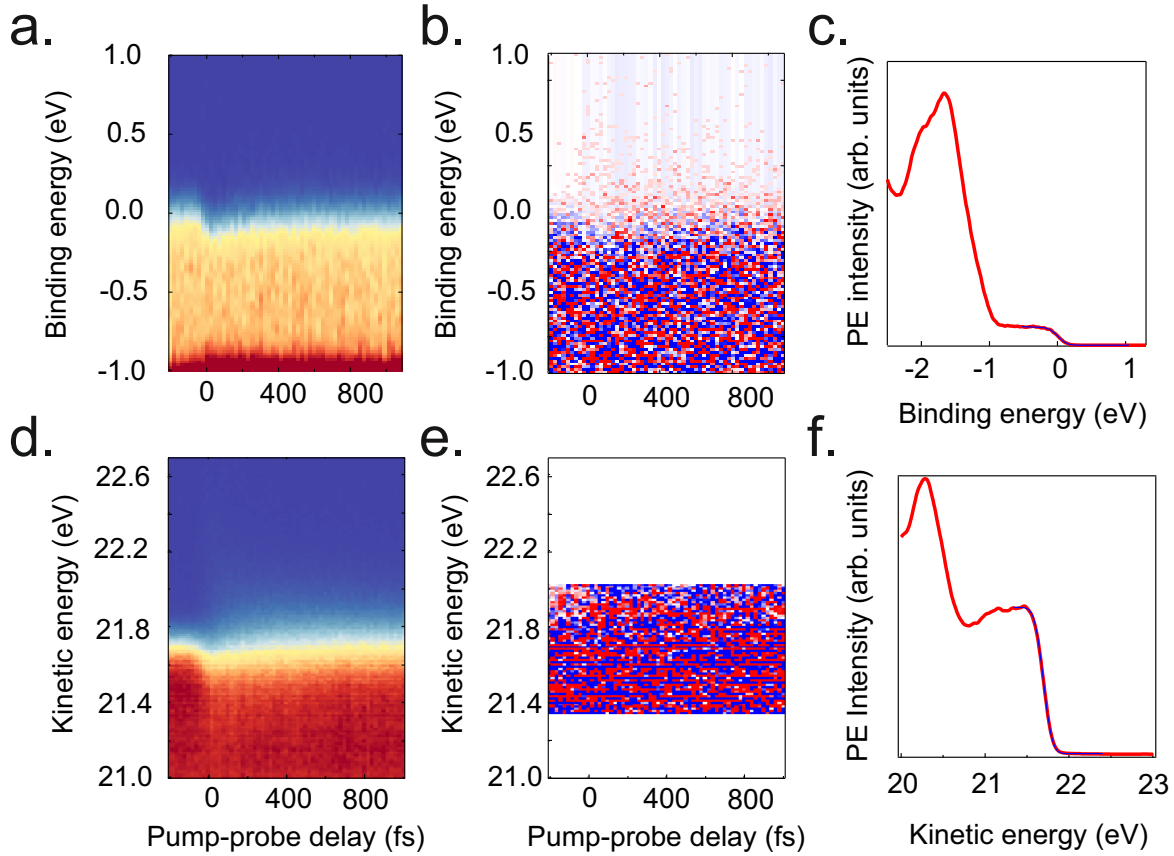
Figure S7: **Fits of the Fermi edge.** a. Surface state Fermi edge dynamics map showing an EDC for every delay. EDCs are extracted integrating k_x [-0.5, 0.5] and k_y [-0.5,0.5] to encompass the Shockley surface state. b. Residuals at each delay, the image colorscale has been scaled to cover $\pm 0.5\%$ of the Fermi edge amplitude. c. Representative EDC (red, solid line) with Fermi edge fit (blue solid line). d. Fermi edge dynamics map showing an EDC for every delay. EDCs are extracted integrating a range including the sp-band. e. Residuals at each delay, the image colorscale has been scaled to cover $\pm 0.3\%$ of the Fermi edge amplitude. f. Representative EDC (red, solid line) with Fermi edge fit (blue solid line).

with

$$P(t) = \frac{A}{\Delta t/2 \cdot \sqrt{\pi/\ln(2)}} \cdot e^{\dfrac{-4\ln(2)(t-t_0)^2}{\Delta t^2}} \tag{3}$$

values of the parameters are $\gamma_e = 70$ Jm^{-3}K^{-2}, $G_{e-ph} = 3 \times 10^6$ Wm^{-3}K^{-1} at 300 K, $G_{e-ph} = 2 \times 10^6$ Wm^{-3}K^{-1} at 70 K, $C_l = 2.4 \times 10^6$ JK^{-1} at 300 K, $C_l = 2 \times 10^6$ JK^{-1}, $A = 10^8$ Vm^{-1}, $\Delta t = 36$ fs.

13   Optical properties and thickness of free-standing WSe$_2$

For the FED experiments we have estimated the thickness of bare WSe$_2$ flakes from their optical properties (absorption spectrum). Subsequently, the thickness of the deposited Au

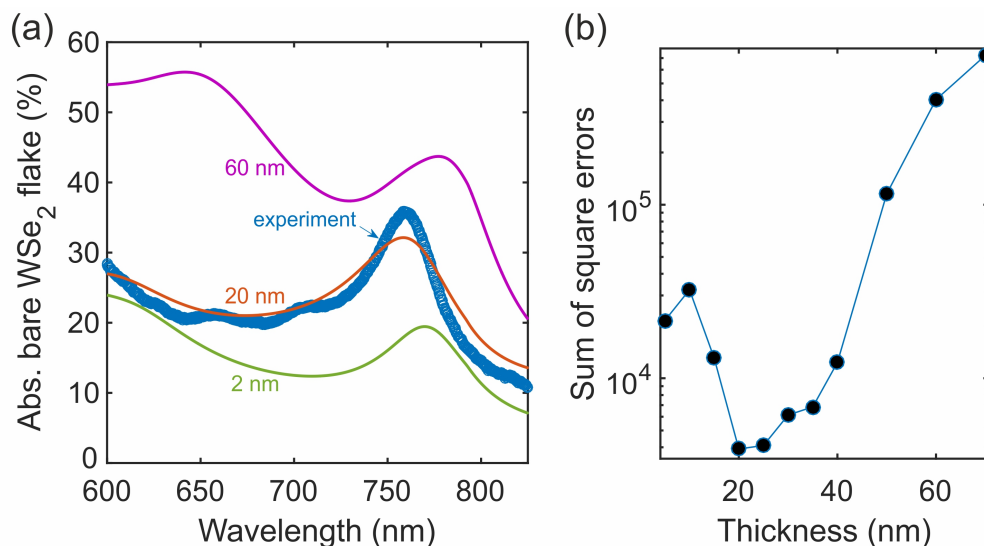(with electron beam evaporation) was controlled with a quartz crystal microbalance.

Figure S8: **Fitting the absorption spectrum of bare WSe₂ flakes used for FED to extract the thickness.** (a) The experimental absorption spectrum of a bare WSe$_2$ represented with the calculated spectra for 20 nm and 30 nm thickness. (b) The sum of square errors (residuals) as a function of the thickness.

The values for the wavelength-dependent real (n) and imaginary (k) refractive indices of multilayer WSe$_2$ are taken from the work of Gu et al.[3]. The absorption spectrum is calculated with the transfer matrix method as a function of the WSe$_2$ thickness. The calculated spectra are compared with the experimental results (Fig. S8 a). The sum of square errors (residuals of the fitting) is minimized for a thickness of 20-25 nm (Fig. S8 b).

14 Extraction of MSD and lattice temperatures from FED

An example of a static diffraction pattern of the Au/WSe$_2$ heterostructures in logarithmic scale is shown in Fig. S9 a. The bright hexagonal pattern corresponds to single-crystalline, multilayer flakes of WSe$_2$. The less intense diffraction pattern corresponds to the epitaxially grown, (111)-oriented, nanoislands of Au (inset of Fig. S9 a). In the time-resolved experiments the lattice dynamics are initiated by femtosecond laser pulse pumping the electrons. The lattice dynamics are probed with ultrashort electron pulses at selected pump-probe delays. For each diffraction peak of WSe$_2$ we extract the relative intensity (Fig. S9 b) and subsequently the change of the atomic MSD (Fig. S9 c). For Au the temporal evolution of the MSD (Fig. S9 d) cannot be described by the single-exponential dynamics measured previously for bulk Au and Au nanoclusters on insulating substrates.

To confirm that sub-band-gap light does not induce any measurable lattice dynamics in bare WSe$_2$, we have performed the experiment shown in Fig. S10 a. First, we found spatial and temporal overlap of pump (850 nm) and probe (electrons), and then we moved to a bare WSe$_2$ flake and repeated the FED scan in the ± 20 ps range.

In contrast, sub-band-gap light initiates a strong lattice response for Au-decorated WSe$_2$ flakes. An incident laser fluence of 0.97 mJ/cm^2 can cause a 410 K temperature rise of the Au nanoislands (Fig. S11 a).The representation of the temperature of evolution of Au with a
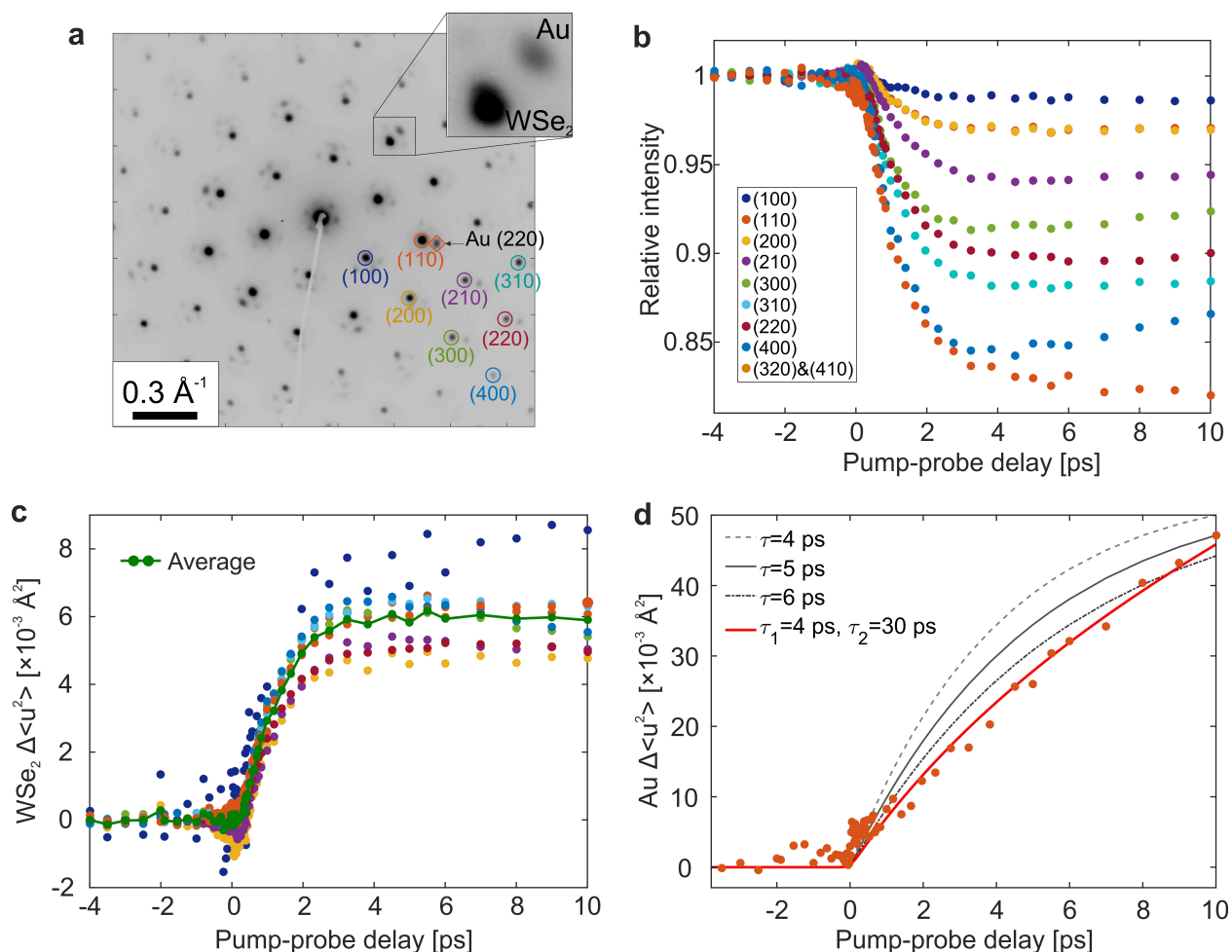
Figure S9: **FED of Au/WSe$_2$ heterostructures pumped at the A-exciton resonance**. (a) The electron diffraction pattern of Au/WSe$_2$ (logarithmic scale). The dark spots represent areas with high intensity of diffracted electrons. The two materials form two hexagonal patterns with strong and weak intensity of diffracted electrons belonging to WSe$_2$ and Au, respectively (see inset). (b) After excitation (Delay¿0) all diffraction peaks decay due to the Debye-Waller effect [18, 19]. The inset shows the index of each diffraction peak. (c) The intensity decay from each diffraction peak is used to extract the time-dependent atomic MSD of WSe$_2$ (same color code as in (a and b) and the average of all peaks (green dot-line). (d) The time-dependent atomic MSD of Au following the same procedure. The solid lines represent exponential decay functions of various time-constants.

biexponential function is 20% more accurate, in terms of the sum of square errors, compared to a single exponential. The two processes have time-constants 4 ps and 16 ps and cause temperature rises of 90 and 310 K, respectively.

Based on the results and discussions of the main article, the fast process is attributed to electron-phonon coupling in Au and the slow process to exciton dissociation. Fig. S11 b shows the temperature rises caused by the two processes as a function of the incident laser fluence. The solid lines are fittings with functions of the form $aF + bF^c$, where F is the fluence. Noticeably, as the fluence increases the heating of Au is dominated by exciton dissociation, while electron-phonon coupling in Au is suppressed. This observation corroborates our conclusion that plasmons and hot electrons in Au can induce nonlinear absorption and
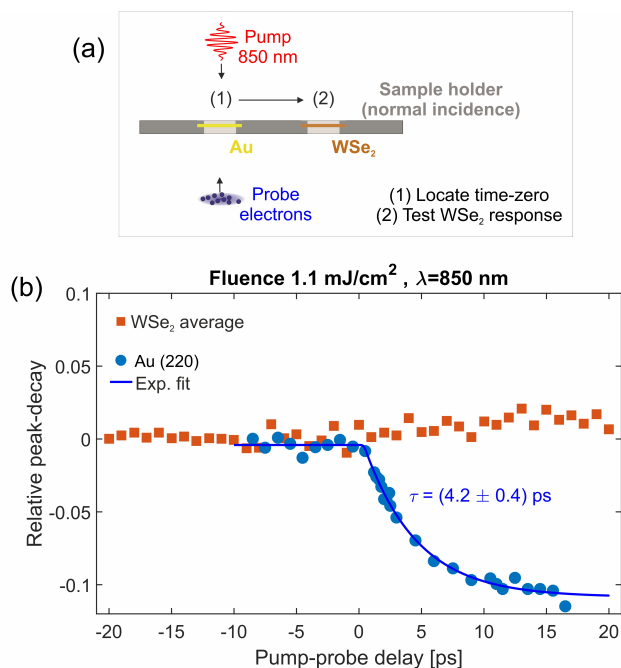
Figure S10: **No lattice response of bare WSe₂ flakes exposed to sub-band-gap light.** (a) The experiment used for finding temporal overlap of pump and probe and then testing the lattice dynamics of bare WSe₂. (b) The relative peak-decay for the (220) peak of a Au thin-film and for the average of the WSe₂ peaks.
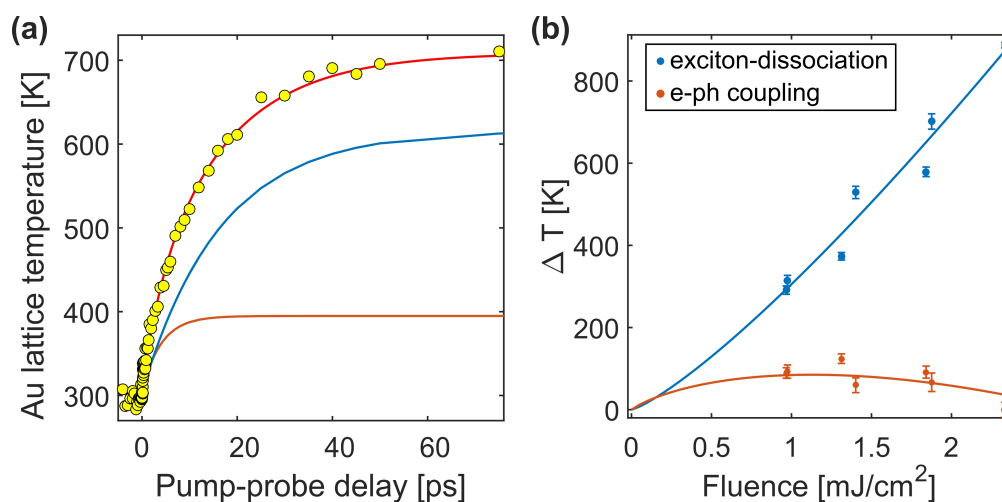

Figure S11: **Lattice temperature evolution of Au nanoislands.** (a) Lattice temperature evolution of Au nanoislands on WSe₂ with sub-band-gap light. The experimental data (points) are fitted with a biexponential function (red) with time-constants 4 ps (orange) and 16 ps (blue). (b) The fluence dependent temperature rises of the fast and slow process, which are attributed to e-ph coupling and exciton dissociation, respectively.

rapid energy transfer into WSe₂.

References

[1] A. Rettenberger, P. Bruker, M. Metzler, F. Mugele, T. W. Matthes, M. Böhmisch, J. Boneberg, K. Friemelt, P. Leiderer, *Surface science* **1998**, *402* 409.

[2] P. B. Johnson, R.-W. Christy, *Physical review B* **1972**, *6*, 12 4370.

[3] H. Gu, B. Song, M. Fang, Y. Hong, X. Chen, H. Jiang, W. Ren, S. Liu, *Nanoscale* **2019**, *11*, 47 22762.

[4] J. J. Mortensen, L. B. Hansen, K. W. Jacobsen, *Physical Review B* **2005**, *71*, 3 035109.

[5] J. Yan, K. W. Jacobsen, K. S. Thygesen, *Physical Review B* **2011**, *84*, 23 235430.

[6] I.-B. Lin, T. W.-H. Sheu, J.-H. Li, *Optics express* **2014**, *22*, 25 30725.

[7] L. Avakyan, V. Durimanov, D. Nemesh, V. Srabionyan, J. Ihlemann, L. Bugaev, *Optical Materials* **2020**, *109* 110264.

[8] A. Bruix, J. A. Miwa, N. Hauptmann, D. Wegner, S. Ulstrup, S. S. Grønborg, C. E. Sanders, M. Dendzik, A. G. Čabo, M. Bianchi, et al., *Physical Review B* **2016**, *93*, 16 165422.

[9] Y. Zhang, O. Pluchery, L. Caillard, A.-F. Lamic-Humblot, S. Casale, Y. J. Chabal, M. Salmeron, *Nano letters* **2015**, *15*, 1 51.

[10] C. M. Smyth, R. Addou, S. McDonnell, C. L. Hinkle, R. M. Wallace, *2D Materials* **2017**, *4*, 2 025084.

[11] M. Massicotte, P. Schmidt, F. Vialla, K. G. Schädler, A. Reserbat-Plantey, K. Watanabe, T. Taniguchi, K.-J. Tielrooij, F. H. Koppens, *Nature nanotechnology* **2016**, *11*, 1 42.

[12] J. R. Dunklin, A. H. Rose, H. Zhang, E. M. Miller, J. Van De Lagemaat, *ACS Photonics* **2019**, *7*, 1 197.

[13] S. Dong, M. Puppin, T. Pincelli, S. Beaulieu, D. Christiansen, H. Hübener, C. W. Nicholson, R. P. Xian, M. Dendzik, Y. Deng, et al., *Natural Sciences* **2021**, e10010.

[14] A. Arora, M. Koperski, K. Nogajewski, J. Marcus, C. Faugeras, M. Potemski, *Nanoscale* **2015**, *7*, 23 10421.

[15] B. Mueller, B. Rethfeld, *Physical Review B* **2013**, *87*, 3 035139.

[16] J. Chen, D. Tzou, J. Beraun, *International Journal of Heat and Mass Transfer* **2006**, *49*, 1 307.

[17] D. C. Ratchford, A. D. Dunkelberger, I. Vurgaftman, J. C. Owrutsky, P. E. Pehrsson, *Nano Letters* **2017**, *17*, 10 6047, pMID: 28850243.

[18] J. Spence, *Acta Crystallographica Section A* **2004**, *60*, 4 355.

[19] H. X. Gao, L.-M. Peng, *Acta Crystallographica Section A* **1999**, *55*, 5 926.